Picosecond acoustic phonon pulse generation in nickel and chromium

T. Saito, O. Matsuda, and O. B. Wright*
Department of Applied Physics, Faculty of Engineering, Hokkaido University, Sapporo 060-8628, Japan
(Received 21 April 2002; revised manuscript received 27 November 2002; published 28 May 2003)

The generation mechanisms for picosecond acoustic phonon pulses excited by ultrashort optical pulses in metals with strong electron-phonon coupling are elucidated. By means of an interferometric probing technique to extract changes in optical phase and amplitude, the acoustic pulse shapes in the transition metals Ni and Cr are shown to be governed by both thermal and nonequilibrium electron diffusion. Quantitative comparison of the results with a model that takes into account the nonequilibrium electron dynamics and ultrasonic attenuation gives excellent agreement.

DOI: 10.1103/PhysRevB.67.205421 PACS number(s): 78.47.+p, 43.35.+d, 66.10.Cb, 63.20.Kr

I. INTRODUCTION

Applying sonar techniques to thin films and nanostructures has become possible using ultrashort optical pulses.[1–9] Acoustic pulses of a few picoseconds in duration, with frequencies typically in the 100 GHz region, can be generated and detected by optical pulse trains focused to areas of a few microns in diameter, allowing the noncontact measurement of internal interfaces or defects. Although research into generation and detection of picosecond acoustic pulses in crystalline semiconductors is still in its infancy,[10] such research on metals is much more advanced: practical applications in the field of multilayer metal thin film evaluation are already well established.[11–13]

For a metal at room temperature the process for the generation of a longitudinal phonon pulse with visible ultrashort light pulses is as follows: the light pulse is absorbed near the metal surface within the optical absorption depth $\zeta \sim 10$ nm. The electrons within the photon energy of the Fermi surface are excited to higher available states. While these hot nonequilibrium electrons diffuse into the sample they transfer their energy to the lattice, a process mediated by the electron-phonon interaction. The final spatiotemporal strain profile of the longitudinal acoustic phonon pulse traveling directly away from the surface is determined by both thermal and electron diffusion. For metals with a relatively small electron-phonon (e-p) coupling constant (~ 20–60×10^{15} W m^{-3} K^{-1}), such as the case of the noble metals or aluminum, the nonequilibrium electrons can diffuse relatively deep into the solid, to distances of ~ 100 nm, before the electrons deposit their energy to the lattice.[14–16] Thermal expansion over this distance determines the dominant wavelength ~ 100 nm of the acoustic pulses that propagate into the metal, with a corresponding central frequency ~ 10 GHz. In these metals the final profile of the longitudinal acoustic strain and the resulting phonon frequency spectrum can be explained accurately by theories accounting for electron diffusion alone.[14–16] For metals with a large e-p coupling constant (~ 200–500 W m^{-3} K^{-1}) this is no longer the case: during the phonon generation heat can diffuse to a depth of the same order as that of the nonequilibrium electrons, and one would therefore expect that both nonequilibrium electron diffusion and thermal diffusion (that is, equilibrium electron diffusion) play a role in determining the acoustic pulse shape. Such ''strong e-p coupling'' metals are of interest because the relatively short diffusion depths (~ 10–20 nm) allow the excitation of much higher frequency acoustic pulses, and so such metals have potential for use as ultrasonic transducers at frequencies >100 GHz.[18,19] This high frequency generation has been experimentally demonstrated in picosecond pulse-echo studies in thin films of Ni,[1,3,2,17] Cr,[20] Mo,[2,4] Ti,[21] Ta,[12] Hf,[9] and W.[4,8,5–7] Acoustic echoes are optically detected through reflectivity changes,[1,4–7] by probe beam deflection,[4] by probe beam diffraction,[3,12] or by interferometry.[8,20] Interferometric methods have the advantage of allowing the simultaneous measurement of optical reflectance and phase changes, giving better experimental access to the actual strain profile of the acoustic pulses.

Such studies present several challenges. (1) Photoelastic effects distort the acoustic echo signals, and the strain pulse shape can only be inferred by self-consistent fitting of strain pulse shapes to the observed echo signals. (2) Ultrasonic attenuation at high frequencies in the 10–100 GHz range can be strongly frequency dependent, and so its effective filtering effect on the acoustic signals must be considered in any accurate analysis in the 100 GHz range. (3) Optical constants of metal films are strongly dependent on sample preparation, and so reference to standard data tables is not necessarily reliable when comparing theory and experiment. For these reasons there has not been, to our knowledge, any rigorous test up to now of the mechanisms governing the optical generation of picosecond acoustic phonon pulses in such strong e-p coupling metals. In this paper, we elucidate the generation mechanisms in such metals by ultrashort-optical-pulse excitation and interferometric probing of carefully characterized thin films of the transition metals Ni and Cr. By accurate quantitative comparison of the results with a theoretical model of the nonequilibrium coupling of the electrons and the lattice, both thermal diffusion and nonequilibrium electron diffusion processes are shown to influence the observed phonon pulse profiles.

II. EXPERIMENT AND RESULTS

We use ultrashort pump and probe light pulses emitted from a mode-locked Ti:sapphire laser operating at central wavelength 830 nm and repetition rate 82 MHz. Picosecond acoustic phonon pulses are excited by frequency-doubled pump light pulses of wavelength $\lambda = 415$ nm (corresponding

to a photon energy of 3 eV). These pump light pulses are chopped at 1 MHz by an acousto-optic modulator, and are focused onto the metal films to a spot diameter $\sim 20\ \mu$m [full width at half maximum (FWHM) diameter for intensity] at an incident angle of $\sim 20°$. After passage through the acousto-optic modulator the pump pulses have a duration of 500 fs (FWHM). An incident pump fluence ~ 0.01 mJ cm^{-2} is chosen to allow a linear theory of the generation process to be valid (as discussed in Sec. III). Weaker, delayed probe light pulses of wavelength $\lambda' = 830$ nm (photon energy 1.5 eV), duration 200 fs, and a fluence $\sim 10\%$ of that of the pump are focused at normal incidence to the same area as the pump beam to a similar spot size, and the transient changes in reflectance and phase of this probe beam are monitored using a Sagnac interferometer setup, described in detail elsewhere.[22] Lock-in detection at the acousto-optic modulation frequency allows relative reflectance changes $\sim 10^{-6}$ to be resolved. Both the reflectance and the phase are sensitive to the acoustic strain in the near-surface region, and so with the probe beam one can optically sample the return of the phonon pulses to the sample surface.

Thin films of polycrystalline Ni and Cr, of thickness 200 and 190 nm, respectively, were prepared on silicon (100) substrates of thickness 0.5 mm by electron beam deposition at a pressure of $\sim 1\times 10^{-3}$ Pa at a rate ~ 0.1 nm s^{-1} for Ni, and ~ 0.6 nm s^{-1} for Cr. The film thicknesses were determined from the temporal separation of the phonon pulses and verified to be accurate by needle profiling.[23] From the background pressure and deposition rates used we estimate that the thin films contain a few atomic percent of oxygen.[24] Impurity concentrations of this order in Ni or Cr do not significantly affect the mechanical or thermal properties at room temperature.[25,26] In particular, the above comparison of needle profiling and phonon pulse data allowed us to verify experimentally that the longitudinal sound velocities were consistent with literature bulk values. The optical constants of the films were carefully characterized by ellipsometry, as described later. The grain size of the films was measured by atomic force microscopy and ultrasonic force microscopy to be ~ 100 nm in both Ni and Cr. The Si (100) substrates were chosen for their flatness: the root mean square surface roughnesses of the bare substrate and the film top surfaces were measured by atomic force microscopy to be $\lesssim 1$ nm and $\lesssim 2$ nm, respectively. This level of roughness does not significantly affect the acoustic echo shape.[10] In addition the film surfaces were parallel to an accuracy of better than 2 μrad, implying a negligible contribution to the broadening of the echoes.[10] Moreover, for the film thicknesses and optical spot diameter used, acoustic diffraction effects are negligible.

The solid curves of Figs. 1(a) and 1(b) show the experimental results for the real (ρ) and imaginary parts ($\delta\phi$) of the relative reflectance change $\delta r/r$ $(=\rho + i\,\delta\phi)$ for the Ni and Cr films. The quantity ρ can also be expressed as $\rho = \delta R/2R$, where $R = r^* r$ is the reflectivity and $\delta\phi$ is the optical phase change. Both metals show a sharp change at delay time $t = 0$ followed by a slow decay. This decay is caused by the near-surface temperature decreasing as heat diffuses into the film.[27] These decay curves can be approxi-

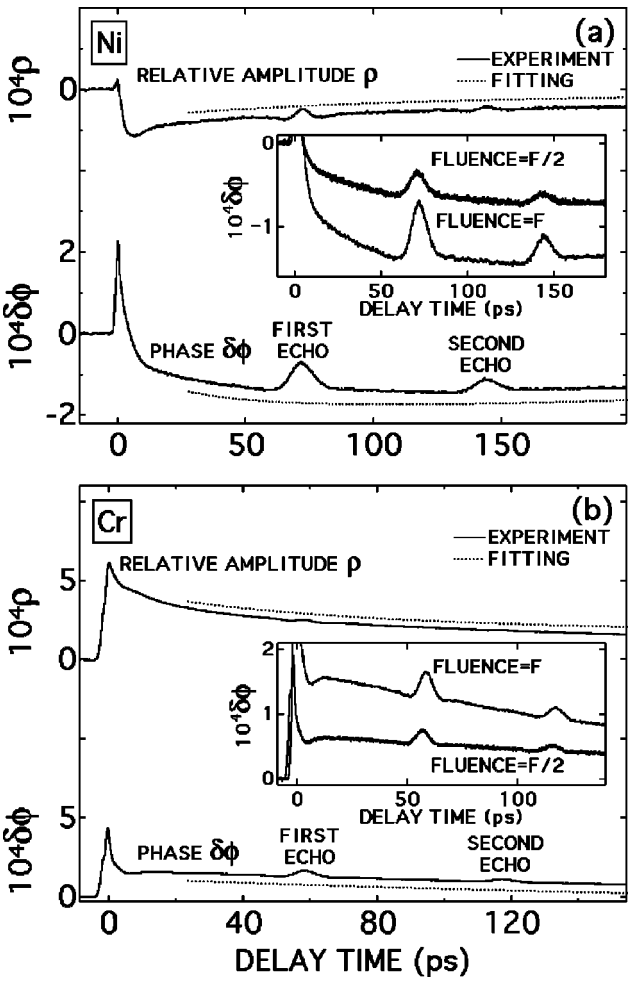

FIG. 1. (a) Experimental amplitude ρ and phase $\delta\phi$ (both shown as solid curves) of the relative reflectance change as a function of delay time for a polycrystalline Ni film of thickness 200 nm on a silicon (100) substrate. The absorbed pump light fluence F for Ni is ~ 0.006 mJ cm^{-2}. The first and second echoes in both ρ and $\delta\phi$ are visible at delay times ~ 70 and ~ 140 ps, respectively. The dotted curves, displaced vertically for clarity, show fits to the thermal background using exponential decays. The inset shows $\delta\phi$ measured at half the incident pump fluence compared with that measured at the full pump fluence on the same scale. (b) Corresponding graph and inset for a Cr film of thickness 190 nm. The absorbed pump light fluence F for Cr is ~ 0.006 mJ cm^{-2}. The first and second echoes in both ρ and $\delta\phi$ are visible at delay times ~ 60 and ~ 120 ps, respectively.

mately reproduced by exponential functions, as shown by the dotted curves in Figs. 1(a) and 1(b). These are empirical fits chosen to leave a flat baseline away from the echoes after subtraction. Superimposed upon this thermal background we observe acoustic echoes caused by longitudinal acoustic phonon pulses reverberating inside the film.

The thin solid curves of Figs. 2(a) and 2(b) show the corresponding first echoes in ρ and $\delta\phi$ with the thermal background [dotted curves in Figs. 1(a) and 1(b)] subtracted. The typical duration of these echoes is ~ 10 ps. The difference in the first and second echoes is caused by the partial acoustic transmission into the substrate and by ultrasonic at-

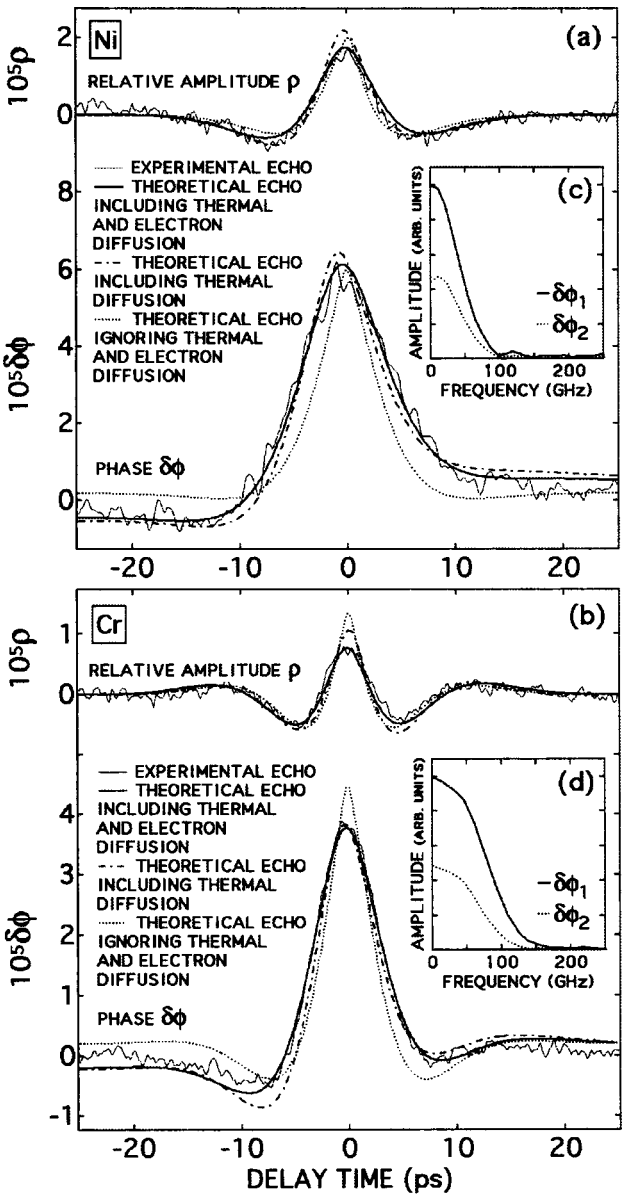

FIG. 2. (a) First echoes for relative amplitude ρ and phase $\delta\phi$ for a 200 nm film of polycrystalline Ni on silicon (100), plotted on identical scales. (b) First echoes for a 190 nm film of Cr on silicon (100). The background thermal decays [dotted curves in Figs. 1(a) and 1(b)] have been subtracted from all four experimental traces (thin solid curves). The thick solid curves are theoretical fits including both thermal and electron diffusion. The dashed-dotted curves correspond to theoretical fits including only thermal diffusion ($g \rightarrow \infty$) and the dotted curves to theoretical fits in the absence of diffusion ($g \rightarrow \infty, \kappa \rightarrow 0$). The theoretical curves include the effect of ultrasonic attenuation, only significant for Cr. (c) The frequency spectra for Ni of the first echo $\delta\phi_1$ and second echo $\delta\phi_2$, calculated from the experimental phase traces in (a). (d) Similar frequency spectra for Cr. The solid curves in (c) and (d) are the spectra of $\delta\phi_1$ and the dotted curves are those for $\delta\phi_2$.

tenuation. Measurements made at half the incident pump fluence showed identical pulse shapes [shown for both Ni and Cr in the insets of Figs. 1(a) and 1(b) on the same scale], demonstrating that the present pump fluences induce a linear sample response. The echoes in ρ have a strongly bipolar shape, and this arises because of the nature of the coupling of the acoustic strain in the near surface region to the real and imaginary components of the refractive index, owing to the photoelastic effect.[1,28] The magnitude of the acoustic strain is $\sim 10^{-4}$ in the present experiments. The echoes in $\delta\phi$ are closer to a unipolar shape, and, as shown previously, are dominated by a contribution from the out-of-plane transient surface motion.[4,3] In our case the magnitude of the surface displacement is ~ 3 pm.

In order to quantify the effects of ultrasonic attenuation we follow the standard procedure of comparing the frequency spectra of the echoes assuming negligible acoustic velocity dispersion,[1] taking into account the partial transmission at the substrate. The amplitude reflection coefficient for the phonon strain pulses from the substrate is expected to be given by $r_{ac}=(\rho_s v_s-\rho_0 v)/(\rho_0 v+\rho_s v_s)$, where ρ_0 is the density, v is the longitudinal sound velocity, and the subscript s refers to the substrate. The values for r_{ac} are -0.42 and -0.43 for Ni and Cr, respectively (see Table I). Figure 2(c) shows the frequency spectrum of the echoes in $\delta\phi$ for Ni calculated from Fig. 2(a), and Fig. 2(d) shows the corresponding spectrum for Cr. Here $\delta\phi_1$ refers to the first echo and $\delta\phi_2$ to the second echo. The spectra show frequency components up to 100 GHz. The ratio of these spectra for Cr indicate an ultrasonic attenuation rising with frequency,[29] whereas the ratio for Ni was independent of frequency over the range probed (up to ~ 100 GHz). That is, the second echo for Ni is the same shape as the first echo to within the experimental resolution. This is consistent with the relatively low value of the ultrasonic attenuation previously measured in the GHz range in Ni.[30] The frequency dependence of the ratio for Cr is used in the following analysis to correct for the effect of acoustic propagation when comparing experiment and theory for the first echo.

III. THEORY AND ANALYSIS BASED ON THE TWO-TEMPERATURE MODEL

In metals thermoelasticity is the dominant mechanism for picosecond acoustic phonon pulse generation.[1,14] A lattice temperature distribution $T_i(z,t)$ is induced by the incident pump light pulse absorbed within a depth $\sim\zeta$, the optical absorption depth. This generates a longitudinal stress distribution $\sigma(z,t)$. Here $\sigma=\sigma_{33}$, and z is the distance into the film, where $z=0$ at the film surface. This one-dimensional approximation for the temperature distribution is reasonable if ζ (~ 15 nm for Ni and Cr) is much smaller than the laser spot size ($\sim 20\ \mu$m), a valid assumption here. The stress pulse can be calculated from a knowledge of the impulsive contributions ($\delta\sigma$) to the stress at points in space and time for which the temperature is varying:

$$\delta\sigma = -\gamma C_i \delta T_i = -3B\beta\delta T_i, \tag{1}$$

where γ is the Grüneisen parameter, B is the bulk modulus, β is the linear thermal expansion coefficient, and C_i is the

TABLE I. Physical constants for Ni and Cr. The refractive indices $\tilde{n}$ and $\tilde{n}'$ are measured by ellipsometry. $dn'/d\eta$ and $dk'/d\eta$ are chosen to give simultaneous best fits to the experimental variations ρ_1 and $\delta\phi_1$, corresponding to the first echo. The density and longitudinal sound velocity of Si (100) are, respectively, $\rho_s = 2.331\ \mathrm{g\,cm^{-3}}$, $v_s = 8433\ \mathrm{ms^{-1}}$ (Ref. 31).

	Ni	Cr
g ($\mathrm{W\,m^{-3}\,K^{-1}}$)	440×10^{15} [a]	420×10^{15} [a]
κ ($\mathrm{W\,m^{-1}\,K^{-1}}$)	91 [b]	94 [b]
v ($\mathrm{ms^{-1}}$)	5894 [c]	6650 [d]
ρ_0 ($\mathrm{g\,cm^{-3}}$)	8.9 [b]	7.2 [b]
$r_{ac}=(\rho_s v_s-\rho_0 v)/(\rho_0 v+\rho_s v_s)$	-0.42	-0.43
C_e/T ($\mathrm{J\,m^{-3}\,K^{-2}}$)	1065 [e]	194 [e]
C_i ($\mathrm{J\,m^{-3}\,K^{-1}}$)	3.95×10^{6} [b]	3.24×10^{6} [b]
$\tilde{n}=n+ik$ at $\lambda=415$ nm	$1.50+2.07i$	$1.74+2.45i$
$\tilde{n}'=n'+ik'$ at $\lambda'=830$ nm	$2.14+3.75i$	$3.27+2.85i$
$\zeta=\lambda/4\pi k$ (nm) at $\lambda=415$ nm	16.0	13.5
$\zeta'=\lambda'/4\pi k'$ (nm) at $\lambda'=830$ nm	17.6	23.2
$z_e=(D_e\tau_e)^{1/2}=(\kappa/g)^{1/2}$ (nm)	14.2	15.0
$\tau_e=C_e/g$ (ps)	0.73	0.14
$D_e=\kappa/C_e$ ($\mathrm{m^2\,s^{-1}}$)	2.42×10^{-4}	6.89×10^{-4}
$z_i=(D\tau_{ac})^{1/2}$ (nm)	8.0	7.7
$\tau_{ac}=\zeta/v$ (ps)	2.8	2.0
$D=\kappa/C_i$ ($\mathrm{m^2\,s^{-1}}$)	2.3×10^{-5}	2.9×10^{-5}
$D/v\zeta$	0.24	0.32
$dn'/d\eta$	1.3 ± 0.1	6.5 ± 0.5
$dk'/d\eta$	-1.2 ± 0.1	-4.1 ± 0.3

[a]Reference 32.
[b]Reference 33.
[c]Reference 34.
[d]Reference 35.
[e]Reference 36.

lattice heat capacity per unit volume. This stress drives a longitudinal strain pulse that eventually travels away from film surface:[14,16]

$$\eta(z,t)=-\frac{3B\beta}{2\rho_0 v^2}\int_{-\infty}^{\infty}dt'\,\mathrm{sgn}[z-v(t-t')]\times\frac{\partial T_i}{\partial t}\Big|_{(|z-v(t-t')|,t')}. \tag{2}$$

This strain pulse includes contributions from the strain traveling towards and reflected from the film surface.

The transient variation $T_i(z,t)$ is affected in general by both thermal and electron diffusion. For time scales greater than the internal electron thermalization time[37] the two-temperature model provides a good simplified description.[38] This implies the separate existence of two temperatures, the electron temperature T_e, and lattice temperature T_i. The temporal and spatial evolution of T_e and T_i are calculated according to two coupled partial differential equations[38]

$$C_e\frac{\partial T_e}{\partial t}=\frac{\partial}{\partial z}\left(\kappa\frac{\partial T_e}{\partial z}\right)-g(T_e-T_i)+\frac{1}{\zeta}S(t)e^{-z/\zeta}, \tag{3}$$

$$C_i\frac{\partial T_i}{\partial t}=g(T_e-T_i), \tag{4}$$

where C_e is the electron heat capacity per unit volume ($C_e\sim0.01C_i$), κ the thermal conductivity, g the e-p coupling constant, and $S(t)$ is the absorbed pump laser power density.[39] Under the present experimental conditions of reasonably low pump fluence F, the temperature dependences of $\kappa\propto T_e/T_i$ and $C_e\propto T_e$ can be ignored.[15,16] (The maximum relative change in T_e is $\sim F/\zeta C_e T_0$ and in T_i is $\sim F/\zeta C_i T_0$. These remain below 0.3 and 0.003, respectively, in the present experiments, where the initial temperature $T_0\sim300$ K.) The temperature dependence of other quantities in these equations is also negligible. According to this model, when an ultrashort laser pulse heating source is introduced through the term $S(z,t)$, the relatively low-heat-capacity electrons initially absorb the photon energy, so that $\Delta T_e\gg\Delta T_i$, where ΔT_e and ΔT_i refer to changes in temperature. The diffusion of these nonequilibrium electrons is characterized by diffusivity $D_e=\kappa/C_e$. As the electrons relax the electron energy is transferred to the lattice, until eventually T_e becomes equal to T_i. The energy relaxation time according to this model is given by $\tau_e=C_e/g$ (typically less than 1 ps for metals), and so the stronger the e-p coupling the faster

the relaxation. [In the limit of $g\rightarrow\infty$, $T_e=T_i$ at all times, and Eqs. (3) and (4) yield the standard equation of Fourier heat diffusion, with heat capacity $C=C_e+C_i$.] After this relaxation, Fourier thermal diffusion with thermal diffusivity $D=\kappa/(C_e+C_i)\approx\kappa/C_i$ is the dominant diffusion process. The large ratio $D_e/D\approx C_i/C_e\sim 100$ implies that nonequilibrium electron diffusion is the dominant transport mechanism for times $\lesssim\tau_e$. For brevity we shall henceforth refer to nonequilibrium electron diffusion as simply electron diffusion in this paper.

With the above linear approximation, Eqs. (3) and (4) can be solved analytically in the frequency domain and, by incorporating the strain generation according to Eq. (2), the frequency spectrum of the acoustic strain pulse can be obtained:[16]

$$\tilde{\eta}(z,\omega)=\frac{3B\beta\tilde{S}(\omega)\omega^2\exp(i\omega z/v)}{\rho_0\kappa v^4(1-i\omega C_i/g)[1+(\zeta\omega/v)^2]}\times\frac{1}{p}\left[\frac{1}{p^2+(\omega/v)^2}+\frac{\zeta^2}{1+\zeta p}\right]. \quad (5)$$

This equation describes the acoustic pulse shape when it has left the near-surface region. Here $\omega/2\pi$ is the acoustic frequency, $\tilde{S}(\omega)$ is the Fourier transform of $S(t)$, and p is defined by

$$p=\left[-\frac{i\omega}{D_e}\left(1+\frac{C_i/C_e}{1-i\omega C_i/g}\right)\right]^{1/2}$$

Equation (5) is fairly complex, but it represents a relatively straightforward process. Before comparing theory and experiment it is useful to make some rough estimates of the length scales involved in electron and thermal diffusion. After the pump pulse arrival and during a time of the order of the energy relaxation time of the electrons $\tau_e=C_e/g$ the nonequilibrium electrons diffuse and transport their energy to a depth $\sim z_e=(D_e\tau_e)^{1/2}=(\kappa/g)^{1/2}$.[14,16] This results in a spatially distributed collection of acoustic sources, giving acoustic pulse broadening (to a temporal duration of $\sim z_e/v$ for $z_e\gtrsim\zeta$).[14] The relative values of z_e and ζ therefore determine the importance of electron diffusion on the picosecond acoustic phonon generation. For both Ni and Cr $z_e\sim\zeta\sim 15$ nm, as shown in Table I, and so electron diffusion significantly affects the generation of acoustic phonon pulses in these metals. Once the electrons have relaxed, the lattice temperature T_i continues to vary because of thermal diffusion. Provided that the thermal diffusivity is reasonably small,[40] the broadening effect of thermal diffusion on the acoustic pulses is roughly determined by thermal diffusion during a time $\tau_{ac}\sim\zeta/v$, equal to the acoustic propagation time across the optical absorption depth. The thermal diffusion length corresponding to this time is given by $z_i=(D\tau_{ac})^{1/2}=(D\zeta/v)^{1/2}$.[41] For both Ni and Cr, $D/\zeta v\sim 0.3$, and $z_i\sim 8$ nm $\sim\zeta/2$. This distance is smaller than the corresponding length z_e for electron diffusion.

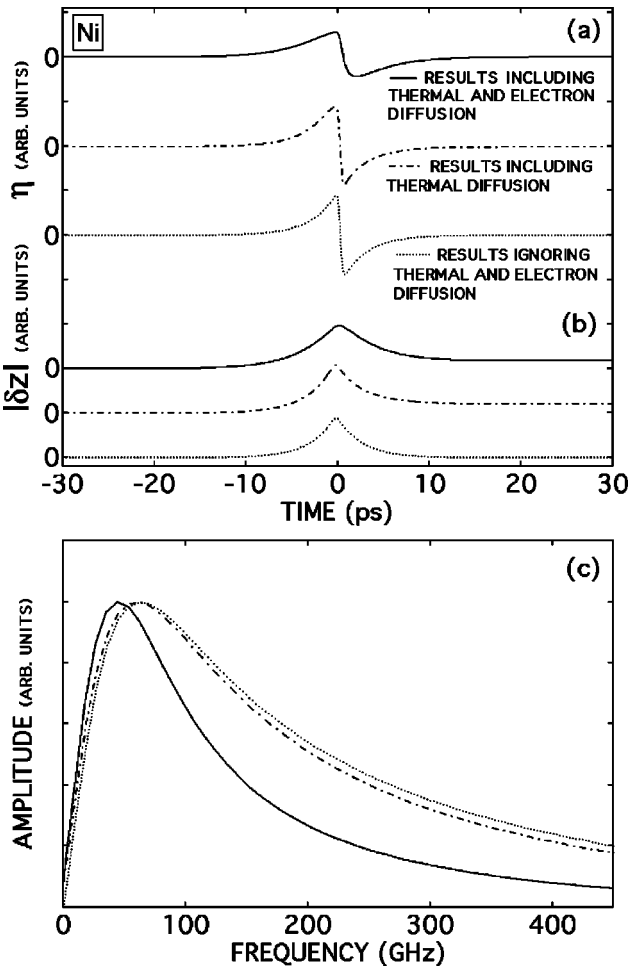

FIG. 3. Calculated profiles in the time domain for (a) the strain pulse η and (b) the inward surface displacement $-\delta z$ for Ni at a position far from the surface in the absence of ultrasonic attenuation (plotted relative to the center of the strain pulse). (c) The strain pulse spectrum for Ni. The solid curve is the strain profile including both thermal and electron diffusion. The dashed-dotted curve is the strain profile including only the effect of thermal diffusion ($g\rightarrow\infty$). The dotted curve is the strain profile in the absence of diffusion ($g\rightarrow\infty$, $\kappa\rightarrow 0$.) The effect of the finite pump and probe pulse durations are included in these curves. The scales are normalized with respect to the heights for no diffusion processes and in the limit of short optical pulse durations.

Quantitative calculations of the strain pulse shape are now given. We show the calculated strain pulse and inward surface displacement $[-\delta z=-\int_0^\infty\eta(z,t)dz]$ variations for Ni in Figs. 3(a) and 3(b). Similar strain and displacement curves were also found for Cr, and are not shown here. The three strain profiles are evaluated numerically by an inverse Fourier transform of Eq. (5). We have used the relevant physical constants from the literature (Table I). In particular, bulk values for the thermal conductivity are used because the grain size of the films is large compared to the diffusion lengths z_e and z_i. The solid curves correspond to the strain pulses including both thermal and electron diffusion, the dashed-dotted curves are the profiles taking into account only thermal diffusion ($g\rightarrow\infty$),[42] and the dotted curves are

the profiles when diffusion is absent ($g\to\infty, \kappa\to 0$). The spatial extent of the picosecond acoustic phonon pulse is broadened by a factor of about 2 by diffusion processes, as seen from the half-width of the displacement pulses. (Because of the effect of the integration to obtain the displacement from the strain, the effect of thermal diffusion on the displacement profiles is more marked than its effect on the strain profiles.) In the frequency domain this corresponds to a peak frequency for the acoustic strain of $\sim$40 GHz compared to $\sim$80 GHz ($\approx v/2\pi\zeta$) in the absence of diffusion. This is clear from Fig. 3(c) where the frequency spectra corresponding to the strain in Fig. 3(b) are shown. Although diffusion processes reduce the peak frequency of the strain pulses, this reduction is much less severe than in the case of the noble metals: for Au, Ag, and Cu the typical peak frequency is $\sim$10 GHz.[14,16,37] The electron-phonon coupling constant in the case of noble metals is typically 10 times smaller than in Ni or Cr, and this accounts for the difference.

IV. COMPARISON OF THEORY AND EXPERIMENT

In order to relate the calculated strain and displacement to quantities measured in experiment it is necessary to calculate the relative variations in optical reflectance $\delta r/r$ for a given $\eta(z,t)$. This can be done by a knowledge of the outward surface displacement $\delta z(t)=\int_0^\infty \eta(z,t)dz$ and the photoelastic constants $d\eta'/d\eta$, $dk'/d\eta$, where $\tilde{n}'=n'+ik'$ is the refractive index at the probe light wavelength λ':[1,22]

$$\frac{\delta r}{r}=\rho+i\,\delta\phi=-i\frac{4\pi}{\lambda'}\delta z+i\frac{8\pi\tilde{n}'}{\lambda'(1-\tilde{n}'^2)}\frac{d\tilde{n}'}{d\eta}\times\int_0^\infty \eta(z,t)\exp\left(i\frac{4\pi\tilde{n}'}{\lambda'}z\right)dz. \qquad (6)$$

The theoretical predictions for ρ and $\delta\phi$, calculated from Eqs. (5) and (6), are shown by the solid curves in Figs. 2(a) and 2(b) for Ni and Cr, respectively. For the case of Cr, where the frequency dependence of the ultrasonic attenuation is significant, its effect is included in these predictions by multiplying the frequency spectrum of the strain in Eq. (5) by the frequency-dependent experimental ultrasonic attenuation factor. The photoelastic constants $d\eta'/d\eta$ and $dk'/d\eta$ are calculated by least-squares fitting, and the refractive indices $\tilde{n}$ and $\tilde{n}'$ are taken directly from measurements by spectroscopic ellipsometry on our thin film samples; other physical constants are taken from the literature (see Table I). We also assume that the temporal intensity variation of the pump and probe pulses are approximated by Gaussian profiles. The ratio of the heights of the echoes in ρ and in $\delta\phi$ are not adjusted relative to one another. Rather, a single adjustable scale factor is used to fit both variations. A variable vertical offset is also included as a fitting parameter to avoid any bias in the choice of a zero level. The zero of the time scale is fixed as the average position of the peaks of the experimental amplitude and phase echoes.[43] The agreement with experiment is optimal with $d\eta'/d\eta\approx 1.3$ and $dk'/d\eta\approx -1.2$ for Ni, and $d\eta'/d\eta\approx 6.5$ and $dk'/d\eta\approx -4.1$ for Cr. These values are, in general, strong functions of the probe wavelength. (The errors in $d\eta'/d\eta$ and $dk'/d\eta$ quoted in Table I refers to an increase of the least-squares residuals by 5%). The absolute magnitude of the echoes in ρ and in $\delta\phi$ are in agreement to within $\sim$50% of those predicted. This agreement is reasonable in view of the uncertainties in the laser spot size diameters and the incident power of the pump laser light.

The dotted curves in Figs. 2(a) and 2(b) correspond to the calculated echoes without including electron and thermal diffusion ($g\to\infty$, $\kappa\to 0$), and the dashed-dotted curves correspond to the calculated echoes including thermal diffusion alone ($g\to\infty$), again calculated using the least-squares technique and including the effect of the experimentally measured ultrasonic attenuation (for Cr). For both Ni and Cr, the theory including both electron and thermal diffusion (solid curves) gives the best agreement with the experimental results.[44]

In this paper we have only considered diffusion effects. On very short time scales $\sim$10–30 fs characteristic of the electron-electron scattering time $\tau_{e\text{-}e}$ for the excited electrons, ballistic electron propagation affects the penetration of the nonequilibrium electrons into the metal.[45,46] In Ni and Cr excited by 3 eV photons, d electrons above the Fermi level are predominantly involved,[47–49] and it is their initial transport at velocities at a substantial fraction[46] of the Fermi velocity v_F that is ballistic. Such ballistic propagation velocities lead to electron transport distances $\sim v_F\tau_{e\text{-}e}\sim$10 nm. A calculation of such corrections to our simpler theoretical approach proposed here is beyond the scope of this paper. However, the present work has shown that in Ni and Cr the two-temperature model, in spite of its simplicity, is successful in quantitatively accounting for the observed echo shapes and hence for the phonon strain pulse shapes.

V. CONCLUSIONS

In conclusion, we have investigated the generation mechanisms for picosecond acoustic phonon pulses excited by ultrashort optical pulses in Ni and Cr, metals with strong electron-phonon coupling. We have analyzed quantitatively the shapes of the acoustic phonon pulses using the linearized two temperature model. Comparison with the experimental optical reflectance and phase changes leads to excellent agreement with this model, taking into consideration the broadening effect of the ultrasonic attenuation (where necessary) calculated from the experimental results. We conclude that both nonequilibrium electron diffusion and thermal diffusion affect the optical generation of picosecond acoustic phonon pulses excited in Ni and Cr. In the future it would be interesting to extend this work to measurements of other transition metals, and to investigate the effect of changing the excitation photon energy on the acoustic strain profiles in order to explore in detail the effect of band structure on phonon generation.

*Electronic address: assp@kino-ap.eng.hokudai.ac.jp

[1] C. Thomsen, H. T. Grahn, H. J. Maris, and J. Tauc, Phys. Rev. B **34**, 4129 (1986).
[2] G. L. Eesley, B. M. Clemens, and C. A. Paddock, Appl. Phys. Lett. **50**, 717 (1987).
[3] T. F. Crimmins, A. A. Maznev, and K. A. Nelson, Appl. Phys. Lett. **74**, 1344 (1999).
[4] O. B. Wright and K. Kawashima, Phys. Rev. Lett. **69**, 1668 (1992).
[5] J. L. Hostetler, A. N. Smith, and P. M. Norris, Microscale Thermophys. Eng. **1**, 237 (1997).
[6] C. J. K. Richardson, M. J. Ehrlich, and J. W. Wagner, J. Opt. Soc. Am. B **16**, 1007 (1999).
[7] A. Devos and C. Lerouge, Phys. Rev. Lett. **86**, 2669 (2001).
[8] B. Bonello, B. Perrin, E. Romatet, and R. Gohier, Proc. Natl. Acad. Sci. U.S.A. **6**, 440 (1996).
[9] K. A. Svinarich, W. J. Meng, and G. L. Eesley, Appl. Phys. Lett. **57**, 1185 (1990).
[10] O. B. Wright, B. Perrin, O. Matsuda, and V. E. Gusev, Phys. Rev. B **64**, 081 202 (2001).
[11] R. J. Stoner, C. J. Morath, G. Tas, S. Sengupta, S. M. Merchant, J. B. Bindell, and H. J. Maris, Proc. SPIE **3269**, 104 (1998).
[12] R. M. Slayton, K. A. Nelson, and A. A. Maznev, J. Appl. Phys. **90**, 3292 (2001).
[13] B. Bonello, B. Perrin, E. Romatet, and J. C. Jannet, Ultrasonics **35**, 223 (1997).
[14] O. B. Wright, Phys. Rev. B **49**, 9985 (1994).
[15] G. Tas and H. J. Maris, Phys. Rev. B **49**, 15 046 (1994).
[16] O. B. Wright and V. E. Gusev, IEEE Trans. Ultrason. Ferroelectr. Freq. Control **42**, 331 (1995).
[17] V. Gusev, J.-M. Breteau, and P. Picart, Ultrasonics **38**, 475 (2000).
[18] T. C. Zhu, H. J. Maris, and J. Tauc, Phys. Rev. B **44**, 4281 (1991).
[19] H. Y. Hao and H. J. Maris, Phys. Rev. B **63**, 224 301 (2001).
[20] D. H. Hurley, O. B. Wright, O. Matsuda, V. E. Gusev, and O. V. Kolosov, Ultrasonics **38**, 470 (2000).
[21] H.-N. Lin, R. J. Stoner, H. J. Maris, J. M. E. Harper, J. C. Cabral, and J. H. G. W. Rubloff, Appl. Phys. Lett. **61**, 2700 (1992).
[22] D. H. Hurley and O. B. Wright, Opt. Lett. **24**, 1305 (1999).
[23] Both film thicknesses are determined from the equation $v\Delta t/2$ using the values of the longitudinal sound velocity v listed in Table I and the temporal interval Δt between the first and second echoes in Figs. 1(a) and 1(b). Needle profiling gave identical thicknesses within the experimental error 200 ± 10 nm for Ni and 190 ± 10 nm for Cr.
[24] A. K. Kulkarni and L. C. Chang, Thin Solid Films **301**, 17 (1997).
[25] *Thermophysical Properties of Matter: Thermal Conductivity: Metallic Elements and Alloys*, edited by Y. S. Touloukian, R. W. Powell, C. Y. Ho, and P. G. Klemens (IFI/Plenum, New York, 1970).
[26] A. R. Wolter, J. Appl. Phys. **36**, 2377 (1965).
[27] C. A. Paddock and G. L. Eesley, J. Appl. Phys. **60**, 265 (1986).
[28] A. M. Z. Bozóki and A. Lörincz, J. Appl. Phys. **66**, 2968 (1989).
[29] The logarithm of this ratio can be used to calculate the ultrasonic attenuation coefficient for Cr. The frequency dependent part of this attenuation coefficient could be fitted by $\alpha\approx190f^2$ in m^{-1}, with f in GHz.
[30] W. Sigle and O. Weis, Z. Phys. B: Condens. Matter **53**, 75 (1983).
[31] *CRC Handbook of Chemistry and Physics*, edited by D. R. Lide, 82nd ed. (CRC Press, Boca Raton, 2001).
[32] T. Q. Qiu and C. L. Tien, Int. J. Heat Mass Transf. **35**, 719 (1992).
[33] *American Institute of Physics Handbook*, edited by D. E. Gray, 3rd ed. (McGraw-Hill, New York, 1972).
[34] O. L. Anderson, *Physical Acoustics: Principles and Methods* (Academic, New York, 1965), Vol. 2.
[35] G. S. Kino, *Acoustic Waves: Devices, Imaging and Analog Signal processing* (Prentice Hall, New Jersey, 1987).
[36] C. Kittel, *Introduction to Solid State Physics*, 7th ed. (John Wiley, New York, 1996).
[37] V. E. Gusev and O. B. Wright, Phys. Rev. B **57**, 2878 (1998).
[38] S. I. Anisimov, B. L. Kapeliovich, and T. L. Perelman, Sov. Phys. JETP **39**, 375 (1974).
[39] The contribution to the thermal conduction owing to incoherent phonon energy transport is very small compared to the electron contribution, and is ignored in Eq. (4).
[40] The condition for relatively small D is that $D/v\zeta\lesssim1$, that is, $z_e\lesssim\zeta$. If D is larger, then one can estimate z_i from the time required for sound to cross the distance z_i, that is $z_i=(Dz_i/v)^{1/2}$, leading to $z_i\sim D/v$.
[41] The importance of the dimensionless parameter $D/v\zeta$ in determining the effect of thermal diffusion was noted in Ref. 1.
[42] The time axes for the strain profiles given in Ref. 10 were inadvertently multiplied by -1. In addition, the vertical scales in Figs. 1 and 2 of that paper should be interchanged.
[43] The theoretical curves are adjusted so that their peaks coincide with this zero. Both experimental and theoretical echoes for Cr have been multiplied by a Hanning (cosine-squared) function in the range -35 ps to 35 ps to allow Fourier transformation.
[44] The residuals from the least-squares fitting for the models with (a) both thermal and electron diffusion, (b) thermal diffusion alone, and (c) no diffusion were in the ratio 1: 1.5: 2.0 for Ni and 1: 1.4: 1.6 for Cr. The photoelastic constants were held fixed at the optimum values determined in the presence of electron and thermal diffusion. Releasing this constraint did not affect the ratio of the residuals significantly. There is an error in the ratio of the photoelastic constants for Cr quoted in our previous paper: T. Saito, O. Matsuda and O. B. Wright, Physica B **316-317C**, 304 (2002).
[45] S. D. Brorson, J. G. Fujimoto, and E. P. Ippen, Phys. Rev. Lett. **59**, 1962 (1987).
[46] R. Knorren, K. H. Bennemann, R. Burgermeister, and M. Aeschlimann, Phys. Rev. B **61**, 9427 (2000).
[47] F. Weling and J. Callaway, Phys. Rev. B **26**, 710 (1982).
[48] E. Colavita, A. Franciosi, D. W. Lynch, G. Paolucci, and R. Rosei, Phys. Rev. B **27**, 1653 (1983).
[49] E. Colavita, A. Franciosi, C. Mariani, and R. Rosei, Phys. Rev. B **27**, 4684 (1983).